

### **PAPER**

### Semiregular tessellation of electronic lattices in untwisted bilayer graphene under anisotropic strain gradients

To cite this article: Zeyu Liu et al 2025 Chinese Phys. B 34 097309

View the article online for updates and enhancements.

### You may also like

- Doping-induced magnetic and topological transitions in Mn<sub>2</sub>X<sub>2</sub>Te<sub>5</sub> (X = Bi, Sb) bilayers
  Wei Chen, , Chuhan Tang et al.
- Regulation strategies of hot carrier cooling process in perovskite nanocrystals
   Zhenyao Tan, , Kexin Xu et al.
- Extremely large magnetoresistance in single-crystalline ZrBi<sub>2</sub>
  Cundong Li, , Binbin Ruan et al.

SPECIAL TOPIC — Moiré physics in two-dimensional materials

# Semiregular tessellation of electronic lattices in untwisted bilayer graphene under anisotropic strain gradients

Zeyu Liu(刘泽宇)<sup>1,2,3,†</sup>, Xianghua Kong(孔祥华)<sup>1,†,‡</sup>, Zhidan Li(李志聃)<sup>1</sup>, Zewen Wu(吴泽文)<sup>1</sup>, Linwei Zhou(周霖蔚)<sup>1</sup>, Cong Wang(王聪)<sup>2,3</sup>, and Wei Ji(季威)<sup>2,3,§</sup>

<sup>1</sup> College of Physics and Optoelectronic Engineering, Shenzhen University, Shenzhen 518060, China
<sup>2</sup> Beijing Key Laboratory of Optoelectronic Functional Materials & Micro-nano Devices, School of Physics, Renmin University of China, Beijing 100872, China

(Received 12 May 2025; revised manuscript received 24 July 2025; accepted manuscript online 14 August 2025)

Two-dimensional (2D) moiré superlattices have emerged as a versatile platform for uncovering exotic quantum phases, many of which arise in bilayer systems exhibiting Archimedean tessellation patterns such as triangular, hexagonal, and kagome lattices. Here, we propose a strategy to engineer semiregular tessellation patterns in untwisted bilayer graphene by applying anisotropic epitaxial tensile strain (AETS) along crystallographic directions. Through force-field and first-principles calculations, we demonstrate that AETS can induce a rich variety of semiregular tessellation geometries, including truncated hextille, prismatic pentagon, and brick-phase arrangements. Characteristic electronic Dirac and flat bands of the lattice models associated with these semiregular tessellations are observed near the Fermi level, arising from interlayer interactions generated by the spatial rearrangement of AB, BA, and SP domains. Furthermore, the real-space observations of electronic kagome, distorted Lieb, brick-like, and one-dimensional stripe lattices demonstrate that AETS enables tunable semiregular tessellation lattices. Our study identifies AETS as a promising new degree of freedom in moiré engineering, offering a reproducible and scalable platform for exploring exotic electronic lattices in moiré systems.

Keywords: moiré bilayer, semiregular tessellation, electronic lattice, density functional theory

PACS: 73.22.-f, 81.05.ue, 68.65.-k, 68.65.Cd

**DOI:** 10.1088/1674-1056/adfb54 **CSTR:** 32038.14.CPB.adfb54

### 1. Introduction

Two-dimensional (2D) moiré bilayers can be formed by stacking atomically thin van der Waals monolayers with a twist angle or modest lattice mismatch. Specific stacking registries generate localized interfacial electronic states that behave as "super-atoms", assembling into periodic lattices whose symmetry can either mirror that of the parent crystals or exhibit entirely new patterns. The inter-superatomic distances in those moiré lattices typically exceed those in conventional atomic crystals, substantially reducing electron kinetic energy between neighboring superatomic sites and resulting in narrower electronic bandwidths. This kinetic energy is further suppressed by the rapid spatial variation of the stacking registry that creates a strong moiré potential, which localizes the electronic wavefunctions and leads to the formation of flat bands. Such reduced kinetic energy magnifies electronelectron interactions, particularly electron correlation effects at the nanoscale, thereby enabling exotic quantum phases that are inaccessible in their bulk or pristine mono- and bilayer counterparts.[1-4] Extensive research has demonstrated these phenomena primarily in graphene, [5-10] h-BN, [11,12] or

Most studied 2D moiré superlattices exhibit regular tessellation lattice patterns, such as triangular, square, and hexagonal lattices, in terms of both geometric and electronic structures. Electron-electron interactions, enhanced by reduced kinetic energies, can further lead to the electronic states of these regular lattices exhibiting more intricate arrangements, such as the kagome lattice. The kagome lattice is a type of semiregular tessellation, also known as Archimedean tessellation (AT), patterns that host characteristic electronic flat and Dirac bands. [19,20] This raises an intriguing question: can other semiregular tessellation lattices, beyond the kagome lattice, be realized within bilayer moiré superlattices, even purely in terms of electronic states? Strain engineering has proven to be an effective in situ tool for tuning electronic properties in both twisted homo-bilayers [2,21,22] and lattice-mismatched heterobilayers. [23] For instance, under a biaxial tensile strain

<sup>&</sup>lt;sup>3</sup> Key Laboratory of Quantum State Construction and Manipulation (Ministry of Education), Renmin University of China, Beijing 100872, China

transition metal dichalcogenides (TMDs),<sup>[13–18]</sup> which have already demonstrated diverse emergent states and electron correlation effects. Well known examples include correlated insulator,<sup>[5–7,11]</sup> superconductivity,<sup>[6,11]</sup> fractional Chern insulator,<sup>[9,18]</sup> and the quantum anomalous Hall effect.<sup>[16,17]</sup>

<sup>†</sup>These authors contributed equally to this work.

<sup>&</sup>lt;sup>‡</sup>Corresponding author. E-mail: kongxianghuaphysics@szu.edu.cn

<sup>§</sup>Corresponding author. E-mail: wji@ruc.edu.cn

<sup>© 2025</sup> Chinese Physical Society and IOP Publishing Ltd. All rights, including for text and data mining, AI training, and similar technologies, are reserved.

http://iopscience.iop.org/cpb http://cpb.iphy.ac.cn

up to 9.9%, a 1.7° twisted BLG was predicted to exhibit a flat band reproducing the one observed in the magic angle (1.08°) t-BLG. [24] For untwisted bilayers, the lattice mismatch between Bi(110) and SnSe(110) in a Bi(110)-11 × 11/SnSe(110)-12 × 12 heterostructure gives rise to strain-induced dimerbuckling domain boundaries in the Bi layer, which in turn produce at least two one-dimensional flat bands near the Fermi level. [25] Very recently, we proposed a gradient-strain untwisted bilayer graphene, in which each layer is subjected to a different biaxial strain. [26] We theoretically found that strain-dependent structural relaxations induce kagome-like geometries, thereby leading to electronic kagome lattices. However, biaxial strain, with preserved symmetries, has so far been limited to kagome-like structures, leaving other semiregular tessellation lattices unexplored.

In this work, we theoretically demonstrate additional semiregular tessellation electronic lattices in moiré bilayers, which are achievable by introducing a different anisotropic epitaxial tensile strain (AETS) into each layer of untwisted bilayer graphene (BLG). Force-field-based structural relaxations and density functional theory (DFT) electronic calculations were used to determine atomic and electronic structures in these BLGs. Under various in-plane (IP) strain conditions, our force-field calculations unveiled significant structural distortions in these BLGs, resulting in a variety of semiregular tessellation lattices beyond the kagome lattice. These lattices, including truncated hextille, prismatic pentagon, and brickphase arrangements, are each characterized by unique interlayer spacing distributions. Subsequent DFT calculations performed on these identified lattices confirmed the existence of flat bands and Dirac bands in their electronic band structures, consistent with their respective tight-binding (TB) models. Spatial distributions of the corresponding electronic states were further visualized to verify these findings.

### 2. Computational methods and models

All structural relaxations were performed using an implementation of force fields, facilitated by the Large Atomic/Molecular Massively Parallel Simulator (LAMMPS). [27] The C–C interactions within each graphene layer were described using a second-generation reactive empirical bond order (REBO) potential, [28] while the interlayer van der Waals interactions were accounted for via the Kolmogorov–Crespi (KC) potential. [29] All atoms were fully relaxed until the residual force per atom was less than  $1.0 \times 10^{-4}$  eV/Å. The optimized lattice constant of a monolayer graphene unit cell is 2.46 Å, highly consistent with experimental values. Density functional theory calculations were performed using the generalized gradient approximation (GGA) with the Perdew–Burke–Ernzerhof (PBE) functional for the exchange–correlation potential, a linear com-

bined atomic orbitals (LCAO) method, and a single-zeta polarized (SZP) atomic orbital basis set as implemented in the RESCU package. [30] The real space mesh resolution was set to 0.35 Bohr, and the convergence criteria for energy and charge density variation per valence electron were set to  $1.0 \times 10^{-5}$  Hartree and  $1.0 \times 10^{-5}$  electron to ensure good numerical convergence. A  $3 \times 3 \times 1$  k-mesh was adopted to sample the Brillouin zone of the supercells in all calculations. A vacuum layer of thicker than 20 Å was employed to avoid interactions among adjacent supercells.

Herein, we theoretically construct moiré superlattices in untwisted BLG by introducing anisotropic epitaxial strains (AES). Each bilayer supercell consists of a monolayer graphene defined by an anisotropically strained 3N-1  $(a_1) \times$  $3N(a_2)$  supercell, stacked on a bottom graphene layer with a mismatched supercell. Building upon the model of gradientstrained BLG with isotropic tensile strains in both layers, [26] we propose four strategies to apply IP AETS, determined by the largest supercell period of the bottom layer: (i) As depicted in Fig. 1(a), the top layer is subjected to anisotropic tensile strain along both lattice axes, while the bottom layer is strained along only one axis, i.e., the superlattice period of the bottom layer is  $3N \times 3N + 1$ , which we call this strained strategy "AETS-2+1-BLG"; (ii) AETS-2+0-BLG [Fig. 1(b)], the bottom layer is non-strained, i.e., the superlattice period of the bottom layer is  $3N + 1 \times 3N + 1$ ; (iii) AETS-1 + 1-BLG [Fig. 1(c)], involves straining only the  $a_1$  lattice axis of top layer and the  $a_2$  lattice axis of bottom layer, i.e., the superlattice period of bottom layer is  $3N \times 3N + 1$ ; (iv) AETS-1 + 0-BLG [Fig. 1(d)], only the  $a_1$  lattice axis of the top layer is strained, i.e., the superlattice period of bottom layer is  $3N \times 3N$ . In addition, if compressive strain is introduced, there will be a total of 16 cases (Table S1), and here we focus on these four tensile strain configurations. The main features of electronic states observed at N = 8 remain stable within a supercell size range of, at least,  $8 \le N \le 21$ . To simplify, models built with N = 8 were primarily used in following discussion, while the geometric structures for N = 11 and N = 12, along with the electronic structure for N = 11, are presented and discussed in Figs. S8 and S9 to illustrate the robustness.

Notably, the AETS is applied along the primitive lattice vectors of the hexagonal lattice of graphene, rather than the simplified orthogonal lattice. Consequently, the bonds between a carbon atom and its three nearest neighbors (C1, C2, and C3) become anisotropic, exhibiting varying lengths and angles, as shown in Fig. 1(e). This application of the AETS along the crystallographic direction completely breaks the fundamental rotational and mirror symmetries inherent to monolayer graphene. The localized symmetry breaking alters the intrinsic Brillouin zone of graphene, as shown in Fig. 1(f), where the Brillouin zone expands from the original black arrow path to half of the first Brillouin zone.

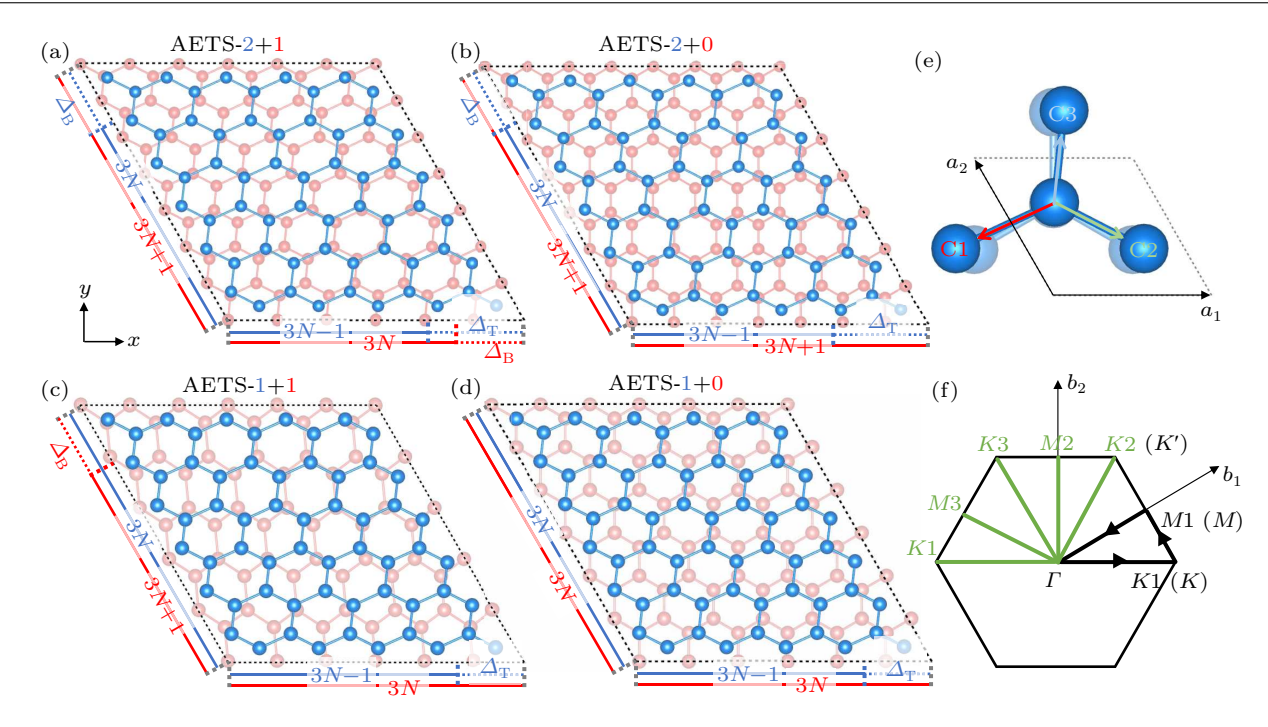


Fig. 1. Schematic models of anisotropic epitaxial tensile strain. (a)–(d) Top views of the models for AETS-(a) 2 + 1-, (b) 2 + 0-, (c) 1 + 1- and (d) 1 + 0-BLG configurations, where the top layer (blue) and bottom layer (red) have graphene supercells in different sizes. The top or bottom layers are subjected to potential strains to ensure that they have the same IP lattice constants in the bilayer supercell. The supercell is marked by the black dashed diamond. (e) Graphene cells subjected to AETS-1 + 0 with anisotropic variations in bond lengths and bond angles. (f) The first Brillouin zone of the AETS-BLGs, with black arrows showing the intrinsic high symmetry path of pristine graphene.

## 3. Geometric and electronic properties of N=8 AETS-BLGs

Building upon the N = 8 superlattice, we explored 16 distinct AES-BLG structures, revealing a rich variety of moiré patterns and stacking orders (Fig. S1). Configurations without compressive strain maintain interlayer spacings within the conventional range for non-strained BLG (3.4-3.6 Å), as shown in Fig. S2. In contrast, introducing compressive strain significantly increases the maximum interlayer spacing to 9.6 Å and induces pronounced out-of-plane (OOP) structural corrugations, consistent with previous reports. [31-33] Despite the presence of such large interlayer separations, the compressively strained bilayers remain structurally stable, as evidenced by a 1 ns NVT molecular-dynamics simulation (see Fig. S3 for more details). This distinction of strain response is highly relevant with strain relaxations. A tensile strain provides atoms with additional space to adopt lower-energy stacking configurations, thereby effectively reducing both intralayer elastic energy and interlayer interaction energy without necessitating OOP relaxation. Conversely, a compressive strain constricts the IP lattice, inducing a strong energetic penalty. To release this strain and minimize the overall energy, atoms are forced to displace out of the plane, effectively redistributing the energy competition between elastic energy (IP and OOP) and stacking energy (OOP).

### 3.1. Geometric structure of AETS-BLGs

Figures 2(a)–2(d) illustrate the fully relaxed atomic structures of the four AETS-BLG configurations for N=8, with each characterizing a distinct set of IP strains. For AETS-2+1-BLG [Fig. 2(a)], the top layer experiences 8.70% and 4.17% tensile strains along the  $a_1$  and  $a_2$  directions, respectively, while the bottom layer undergoes a 4.17% tensile strain along  $a_1$ . In AETS-2+0-BLG [Fig. 2(b)], only the top layer is strained, receiving the same strains as the top layer of AETS-2+1-BLG. For AETS-1+1-BLG [Fig. 2(c)], both layers are subjected to a 4.35% tensile strain, but along different lattice axes ( $a_1$  in the top layer,  $a_2$  in the bottom layer), and finally, for AETS-1+0-BLG [Fig. 2(d)] only the top layer experiences a 4.35% tensile strain.

AETS-BLG moiré superlattices exhibit six high-symmetry stacking configurations: AA, AB, BA, SP1, SP2, and SP3, as depicted in the right side of Fig. 2(d). In the AA stacking (highlighted by a blue circle), each carbon atom in the top layer sits directly above a carbon atom in the bottom layer. A relative lateral sliding by half a unit produces either the AB (purple) or BA (orange) stacking. Applying anisotropic epitaxial strains breaks the intrinsic  $C_3$  rotational symmetry of the graphene. This symmetry breaking lifts the degeneracy of the original SP (saddle-point) stacking (green), causing the SP points to split into three distinct stacking configurations: SP1 (short dashed line), SP2 (long dashed line) and SP3 (solid line). The fully relaxed AETS-2+1, 2+0, and 1+1-BLG structures display patterns combining deformed

hexagonal (AB and BA) and triangular (AA) lattices, as depicted in Figs. 2(a)–2(c). The AETS-1+0-BLG exhibits a distinct stripe pattern composed of alternating AB, SP2, BA,

SP1 regions [Fig. 2(d)]. This specific configuration does not feature AA and SP3 stackings because the epitaxial strain is exclusively applied along the zigzag direction.

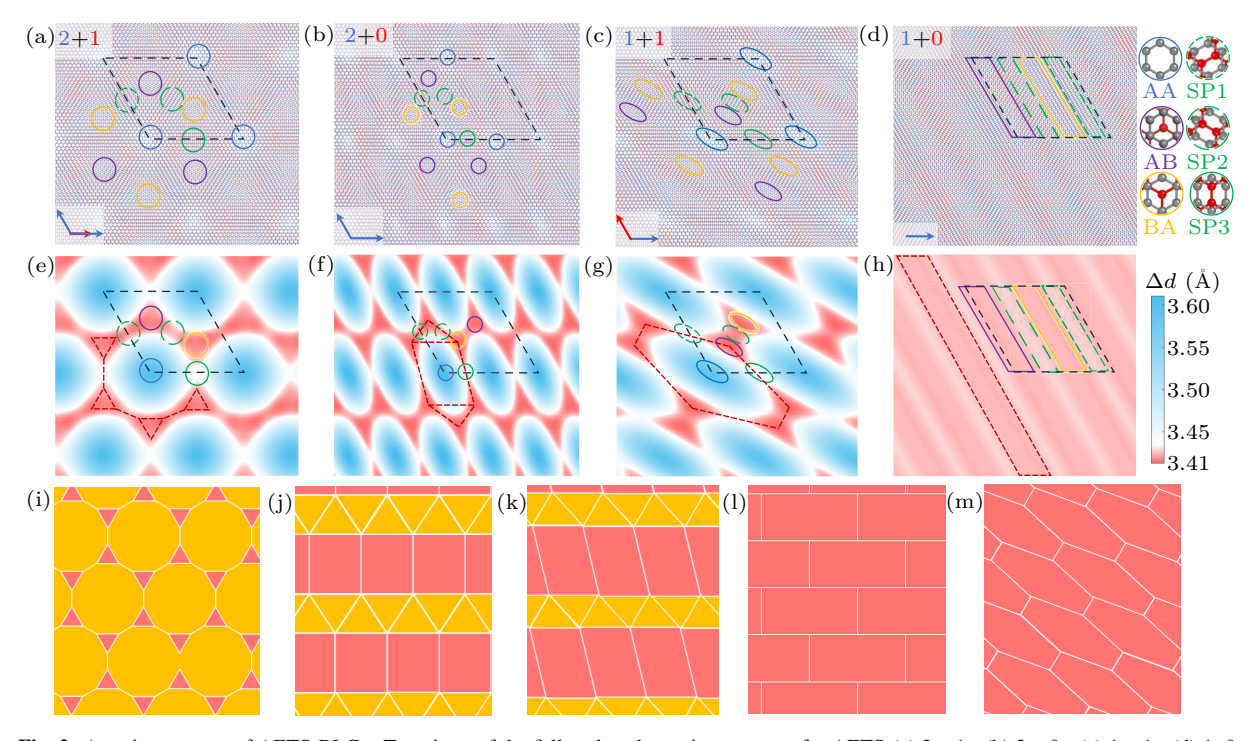


Fig. 2. Atomic structure of AETS-BLGs. Top views of the fully relaxed atomic structures for AETS-(a) 2+1-, (b) 2+0-, (c) 1+1-, (d) 1+0-BLG configurations. The blue and red arrows in the lower left corner represent the top and bottom layers subjected to strain directions. Atomic models on the right side of (d) are presented for these six stacking orders inside the circles with associated colors. (e)–(h) Corresponding maps of the interlayer spacing for each configuration. In the color bar, white represents the optimal interlayer spacing of non-strained SP stacking. (i) An Archimedean tessellation composed of truncated hexagons. Panels (j) and (l) show prism-shaped pentagonal and brick-phase tessellations. Panels (k) and (m) plot the corresponding distorted tessellations patterns for (j) and (l). The supercell is marked by the black dashed diamond, and within the diamond, six high-symmetry stacking orders are denoted by differently colored circles.

Different combinations of IP strains significantly reshape the spatial periodicity of local stacking registries, and induce OOP structural corrugations, leading to distinct interlayer spacing  $(\Delta d)$  distribution patterns. Figures 2(e)-2(h) display the interlayer spacing maps for the four AETS-BLG configurations. In these maps, white regions correspond to the optimal interlayer spacing of non-strained SP stacking, which distinguishes the AA from AB/BA stacking regions. In both AETS-2+1 and -2+0-BLG, the SP1 and SP2 stacking regions form continuous areas, while the SP3 regions are spatially separated. In AETS-1 + 1-BLG, all three SP regions are spatially separated, and the structural anisotropy between the AB and BA regions becomes more pronounced. By contrast, the AETS-1 + 0-BLG exhibits negligible OOP structural corrugation, a direct consequence of the absence of AA stacking in this configuration.

Furthermore, for different AETS-BLG configurations, the AB and BA stacking domains with strong interlayer coupling form four novel semiregular tessellation patterns in the OOP structural distortion mappings. These patterns include a truncated hextille for AETS-2 + 1-BLG [Fig. 2(e)], a prismatic pentagon for AETS-2 + 0-BLG [Fig. 2(f)], a brick phase for AETS-1 + 1-BLG [Fig. 2(g)], and a 1D stripe arrangement

for AETS-1 + 0-BLG [Fig. 2(h)]. Each of these patterns is visually delineated by red dashed triangles and lines in the corresponding figures. Among these, the truncated hextille [Fig. 2(i)] pattern is an AT formed by truncating each vertex of a regular hexagonal lattice, resulting in a two-tile pattern of regular dodecagons (yellow) and equilateral triangles (red), corresponding to a (3.12.12) AT. Similarly, the prismatic pentagon tiling [Fig. 2(j)] is a (3.3.3.4.4) AT composed of pentagons, each pentagon is formed by adjoining an equilateral triangle to a rectangle, which becomes distorted under the AETS-2+0 strain [Fig. 2(k)]. The brick-wall tiling [Fig. 2(1)], corresponding to a (4.4.4) AT, comprises identical rectangular bricks arranged in offset rows, which is also distorted under the AETS-2+0 strain [Fig. 2(m)]. The formation of these interlayer-spacing patterns is driven by a competition between the IP elastic (strain) energy and the interlayer coupling energy. Specifically, in the plane, the system minimizes its elastic (strain) energy by contracting the energetically unfavorable AA regions and expanding the favorable AB/BA regions. Out of the plane, AA regions lower the interlayer coupling energy by increasing the interlayer spacing to approximately 3.6 Å, whereas AB/BA regions maintain interlayer distances close to that of intrinsic Bernal stacking in graphite ( $\sim 3.4 \text{ Å}$ ), in agreement with previously reported observations. [34,35]

### 3.2. Electronic properties in AETS-BLGs

Those semiregular tessellation lattices observed in Figs. 2(e)-2(h) are not merely structural curiosities; they are expected to host exotic electronic states. Specifically, tight-binding (TB) model calculations already predicted characteristic features of these lattices, such as flat and Dirac bands. [20,36-38] For these AETS-BLGs, our DFT calculations explicitly verify this prediction. Figure 3(a) displays the layerprojected band structures of AETS-2 + 1-BLG, highlighting two sets of kagome-derived bands that feature both Dirac and flat band characteristics. The green set of kagome bands comprises two Dirac bands (DP1-A and DP1-B) and a higherenergy flat band (FB1), with states primarily localized in the top layer. In contrast, the brown set includes a lower-energy flat band (FB2) and another two Dirac bands (DP2-A and DP2-B), predominantly distributing in the bottom layer. Dirac bands DP1 (in green) arise from inter-site hopping of the confined states, while Dirac bands DP2 (in brown) are folded from the primitive cell of graphene, as further discussed in Fig. S5. Notably, the two Dirac bands of either DP1 or DP2 do not cross to form a Dirac point, leaving an open energy gap, due to the breaking of  $C_3$  symmetry [Figs. S4(a) and S4(b)]. Moreover, the different relative position of the two flat bands possesses opposite signs of their effective hopping parameters. The interlayer real-space wavefunction norm squared  $|\varphi|^2$  further reveals the intimate connection between these characteristic electronic bands and their underlying lattice models. Figure 3(e) displays the  $|\varphi|^2$  for FB1 at the K point [marked with the green dot in Fig. 3(a)]. Besides the AB and BA stacking regions, the wavefunctions are highly localized also in the SP1, SP2, and SP3 stacking regions. These localized wavefunctions form an electronic kagome lattice, further confirming the kagome flat bands observed in the bandstructure of AETS-2+1-BLG.

Similarly, in AETS-2+0-BLG, two sets of Dirac and flat bands (DP1 + FB1 and DP2 + FB2) are also observed near the Fermi level, as shown in Fig. 3(b). Because the bottom layer remains non-strained, its  $C_3$  rotation symmetry is preserved, ensuring its Dirac bands crossing at the K point. The degeneracy between the flat and Dirac bands at the G point is lifted, with the position of the flat band shifting towards the Dirac point. This behavior is reminiscent of the band structure evolution during a kagome-to-Lieb lattice transition, wherein the flat band shifts from the top/bottom of the Dirac bands (kagome) to the middle (Lieb).[38] This analogy is further strengthened by the  $|\varphi|^2$  of FB1 [Fig. 3(f)], the localization regions (AB, BA, and SP3, in red dots) connect in real space to form a prismatic pentagon lattice (red dashed lines). The outward displacement of the AB-stacked site, relative to the lines linking the BA and SP3 stacked sites, leads to the asymmetric nearest-neighbor hopping amplitudes, forming a distorted Lieb lattice. This observation indicates a strain-tunable transition from an electronic kagome-to-Lieb lattice (Fig. S6).

Figure 3(c) presents the band structure of AETS-1 + 1-BLG, revealing two Dirac and two flat bands near the Fermi level (highlighted in green). The Dirac bands are primarily distributed in the top layer, while the flat bands are contributed by both layers. Because the strain directions of the top and bottom layers are along G–K1 and G–K3, as shown in Fig. S7(c), the same band features also exist in the G–K3 path, while the Dirac bands mainly originate from the bottom layer. Interestingly, epitaxial strain opens an energy gap of approximately 9 meV along G–K1 in monolayer graphene, as depicted in Fig. S4(e). In bilayer graphene, however, the formation of a brick-like lattice composed of AB/BA domains restores the mirror symmetry, closing this small gap. Figure 3(g) presents the  $|\varphi|^2$  of the Dirac band at the K point. Unlike the previous cases, the aggregation of  $|\varphi|^2$  is not localized on specific high-symmetry stacking regions. Instead, it is confined near the edges (red dashed lines) surrounding the AB, BA, and SP2 stacking regions, forming a brick-phase lattice. Combined with the characteristic bands observed in the band structure, this further confirms the emergence of an electronic brick-like lattice modulated by epitaxial strain.

For AETS-1 + 0-BLG, the Dirac bands near the Fermi level are reconstructed and the Dirac point disappears, as shown in Fig. 3(d). This phenomenon is attributed to the strong interlayer coupling within the 1D striped moiré superlattice formed by AB, BA, and SP regions. Moreover, this strong interlayer coupling also induces a pronounced anisotropy in the band dispersion along other high-symmetry paths [Fig. S7(d)]. The  $|\varphi|^2$  of the Dirac band at the K point is modulated by the striped periodic potential and is confined within the SP2 stacking regions, forming a stripe lattice, as shown in Fig. 3(h). The stacking regions within the moiré superlattice, where the electronic wavefunctions localize, can be regarded as effective "superatomic sites". As the AETS varies, these sites redistribute to form semiregular tessellated electronic lattices hosting flat bands, such as kagome, distorted Lieb and brick-phase lattices. The formation mechanism of flat bands here differs fundamentally from those reported in monolayer systems, such as the quantum confinement effect at the "outermost vertices" in a dodecagonal quasicrystal cluster, [39] and the spin-orbit coupling-induced electronic states at kagome-boundary bismuthene. [40] In contrast, AETS-BLGs consist of bilayer graphene without spin-orbit coupling, where anisotropic strain induces both a moiré potential and local lattice distortions, creating superatomic sites through interlayer interactions. Specifically, in the AETS-2+1 and 2+0-BLG models, the flat bands arise from destructive interference of the wavefunctions within the semiregular tessellated lattice of superatomic sites.

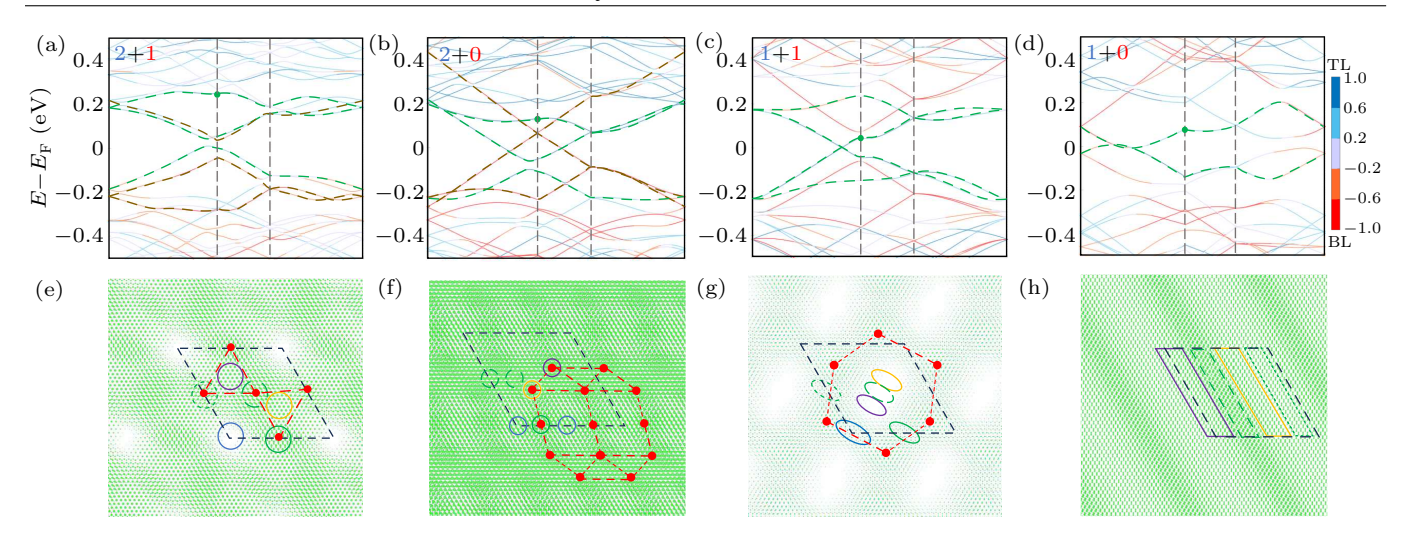


Fig. 3. Electronic properties of AETS-BLGs. (a)–(d) Layer atomic projection energy band diagrams for AETS-2+1-, AETS-2+0-, AETS-1+1-, and AETS-1+0-BLGs. The color bar on the right side of (d) indicates the weight distribution between the top and bottom layers on the projection band. Gray-blue colored lines represent bands combinedly contributed from both the top layer and bottom layer, while the light blue and orange lines indicate dominance by the top layer and bottom layer. Darker blue (red) lines signify nearly exclusive contribution from the top (bottom) layer. The dashed lines highlight one or two sets of characteristic bands for the lattice model. (e) and (f) Plot of interlayer  $|\phi|^2$  for the flat bands (green dots) shown in (a) and (b), where the isosurface values of the wavefunctions are  $3 \times 10^{-5} \ e \cdot Å^{-3}$  and  $1 \times 10^{-5} \ e \cdot Å^{-3}$ . (g) and (h) Plot of interlayer  $|\phi|^2$  for the Dirac bands (green dots) shown in (c) and (d), where the isosurface values of the wavefunctions are  $6 \times 10^{-5} \ e \cdot Å^{-3}$  and  $3 \times 10^{-5} \ e \cdot Å^{-3}$ . Black dashed diamonds and differently colored circles represent the supercell and the six stacking orders in the same scheme used in Fig. 2.

### 4. Conclusion

In summary, we demonstrate that anisotropic epitaxial strain provides a powerful and tunable route for engineering semiregular tessellation of electronic lattices in 2D moiré bilayers. Employing fully atomistic relaxations, we show that IP AETS efficiently induces a redistribution of the interlayer stacking orders, leading to diverse semiregular tessellation patterns, such as truncated hextille, prismatic pentagon, and brick-phase arrangements. Our first-principles calculations further reveal that beyond the kagome electronic lattice structures previously observed under isotropic strain, distinctive electronic bands corresponding to distorted Lieb and brickphase lattices emerge near the Fermi level. These emergent electronic lattices directly correspond to the real-space tessellation patterns. This correspondence stems from the spatial redistribution of strongly coupled AB/BA and SP stacking domains, which in turn generates distinct interlayer interactions. The localized interlayer electronic states that compose these electronic lattices thus confirm the formation of novel topological lattices defined by the geometric patterns. Additionally, we find that the prismatic pentagon pattern observed in AETS-2+0-BLG yields electronic band structures featuring signatures of a distorted Lieb lattice, indicating AETS as an effective means to drive the evolution from kagome to Lieb lattice structures. Recent experimental advances suggest that such anisotropic strains can be realized by employing hetero-substrates<sup>[41]</sup> with flexible polymers<sup>[42]</sup> or highthermal-expansion metal substrates<sup>[43]</sup> as the top and bottom layers, and by nanoscale patterning techniques such as bubbleinduced curvature. [44,45] Collectively, this study establishes anisotropic epitaxial strain as a generalizable degree of freedom in moiré materials design, offering a novel pathway for exploring other (semi-)regular tessellation lattices.

### Acknowledgments

We thank Dr. Kui Gong, Dr. Yibin Hu, and Dr. Yin Wang (all from HZWTECH) and Prof. Yiqi Zhang for helpful discussions. This project was supported by the National Natural Science Foundation of China (Grant Nos. 52461160327, 92477205, 12474173, and 12104313), the National Key R&D Program of China (Grant No. 2023YFA1406500), the Department of Science and Technology of Guangdong Province (Grant No. 2021QN02L820), Shenzhen Science and Technology Program (Grant No. RCYX20231211090126026, the Stable Support Plan Program 20220810161616001), the Fundamental Research Funds for the Central Universities, and the Research Funds of Renmin University of China (Grant No. 22XNKJ30). Calculations were performed at the Physics Lab of High-Performance Computing (PLHPC) and the Public Computing Cloud (PCC) of Renmin University of China.

#### References

- Andrei E Y, Efetov D K, Jarillo-Herrero P, MacDonald A H, Mak K F, Senthil T, Tutuc E, Yazdani A and Young A F 2021 Nat. Rev. Mater. 6 201
- [2] Sinner A, Pantaleon P A and Guinea F 2023 Phys. Rev. Lett. 131 166402
- [3] Tian Z Y, Li S Y, Zhou H T, Jiang Y H and Mao J H 2025 Chin. Phys. B 34 027301
- [4] Han J, Lai K, Yu X, Chen J, Guo H and Dai J 2023 Chin. Phys. Lett. 40 067801
- [5] Cao Y, Fatemi V, Demir A, Fang S, Tomarken S L, Luo J Y, Sanchez-Yamagishi J D, Watanabe K, Taniguchi T, Kaxiras E, Ashoori R C and Jarillo-Herrero P 2018 Nature 556 80

- [6] Saito Y, Ge J, Watanabe K, Taniguchi T and Young A F 2020 Nat. Phys. 16 926
- [7] Choi Y, Kemmer J, Peng Y, Thomson A, Arora H, Polski R, Zhang Y, Ren H, Alicea J and Refael G 2019 Nat. Phys. 15 1174
- [8] Cao Y, Fatemi V, Fang S, Watanabe K, Taniguchi T, Kaxiras E and Jarillo-Herrero P 2018 Nature 556 43
- [9] Xie Y, Pierce A T, Park J M, Parker D E, Khalaf E, Ledwith P, Cao Y, Lee S H, Chen S, Forrester P R, Watanabe K, Taniguchi T, Vishwanath A, Jarillo-Herrero P and Yacoby A 2021 Nature 600 439
- [10] Ding D, Niu R, Han X, Qu Z, Wang Z, Li Z, Liu Q, Han C and Lu J 2023 Chin. Phys. B 32 067204
- [11] Xian L, Kennes D M, Tancogne-Dejean N, Altarelli M and Rubio A 2019 Nano Lett. 19 4934
- [12] Walet N R and Guinea F 2021 Phys. Rev. B 103 125427
- [13] Zhou J, Kong X, Sekhar M C, Lin J, Le Goualher F, Xu R, Wang X, Chen Y, Zhou Y, Zhu C, Lu W, Liu F, Tang B, Guo Z, Zhu C, Cheng Z, Yu T, Suenaga K, Sun D, Ji W and Liu Z 2019 ACS Nano 13 10929
- [14] Kennes D M, Claassen M, Xian L, Georges A, Millis A J, Hone J, Dean C R, Basov D N, Pasupathy A N and Rubio A 2021 Nat. Phys. 17 155
- [15] Mak K F and Shan J 2022 Nat. Nanotechnol. 17 686
- [16] Serlin M, Tschirhart C, Polshyn H, Zhang Y, Zhu J, Watanabe K, Taniguchi T, Balents L and Young A F 2020 Science 367 900
- [17] Li T, Jiang S, Shen B, Zhang Y, Li L, Tao Z, Devakul T, Watanabe K, Taniguchi T, Fu L, Shan J and Mak K F 2021 Nature 600 641
- [18] Yu J, Herzog-Arbeitman J, Wang M, Vafek O, Bernevig B A and Regnault N 2024 Phys. Rev. B 109 045147
- [19] Park D, Park C, Yananose K, Ko E, Kim B, Engelke R, Zhang X, Davydov K, Green M, Kim H M, Park S H, Lee J H, Kim S G, Kim H, Watanabe K, Taniguchi T, Yang S M, Wang K, Kim P, Son Y W and Yoo H 2025 Nature 641 896
- [20] Ohgushi K, Murakami S and Nagaosa N 2000 Phys. Rev. B 62 R6065
- [21] Escudero F, Sinner A, Zhan Z, Pantaleón P A and Guinea F 2024 Phys. Rev. Res. 6 023203
- [22] Bi Z, Yuan N F Q and Fu L 2019 Phys. Rev. B 100 035448
- [23] Kögl M, Soubelet P, Brotons-Gisbert M, Stier A V, Gerardot B D and Finley J J 2023 npj 2D Mater. Appl. 7 32
- [24] Li Y, Yuan Q, Guo D, Lou C, Cui X, Mei G, Petek H, Cao L, Ji W and Feng M 2023 Adv. Mater. 35 2300572
- [25] Li S, Shi X, Li J, He C, Ouyang T, Tang C and Zhong J 2025 J. Appl. Phys. 137 083902

- [26] Liu Z, Kong X, Wu Z, Zhou L, Qiao J, Wang C, Lau S P and Ji W 2025 Nanoscale Horiz. 10 1956
- [27] Plimpton S 1995 J. Comput. Phys. 117 1
- [28] Brenner D W, Shenderova O A, Harrison J A, Stuart S J, Ni B and Sinnott S B 2002 J. Phys.: Condens. Matter 14 783
- [29] Kolmogorov A N and Crespi V H 2005 Phys. Rev. B 71 235415
- [30] Michaud-Rioux V, Zhang L and Guo H 2016 J. Comput. Phys. 307 593
- [31] Argentero G, Mittelberger A, Reza Ahmadpour Monazam M, Cao Y, Pennycook T J, Mangler C, Kramberger C, Kotakoski J, Geim A and Meyer J C 2017 Nano Lett. 17 1409
- [32] Mao Y, Wang W L, Wei D, Kaxiras E and Sodroski J G 2011 ACS Nano 5 1395
- [33] Wang J and Tosatti E 2024 Proc. Natl. Acad. Sci. USA 121 e2418390121
- [34] Borysiuk J, Sołtys J and Piechota J 2011 J. Appl. Phys. 109 093523
- [35] Ould Ne M L, Boujnah M, Benyoussef A and Kenz A E 2016 J. Supercond. Nov. Magn. 30 1263
- [36] Oliver C, Nabari D, Price H M, Ricci L and Carusotto I 2023 arXiv:2310.18325 [physics.optics]
- [37] Liu Y, Wang Y, Hu N C, Lin J Y, Lee C H and Zhang X 2020 Phys. Rev. B 102 035142
- [38] Jiang W, Kang M, Huang H, Xu H, Low T and Liu F 2019 Phys. Rev. B 99 125131
- [39] He C, Li S, Zhang Y, Fu Z, Li J and Zhong J 2025 Phys. Rev. B 111 L081404
- [40] Li S, Shi X, Li J, He C, Ouyang T, Tang C and Zhong J 2024 Phys. Rev. B 110 115115
- [41] Yao F, Rossi D, Gabrovski I A, Multian V, Hua N, Watanabe K, Taniguchi T, Gibertini M, Gutiérrez-Lezama I, Rademaker L and Morpurgo A F 2024 Nat. Commun. 15 10377
- [42] Jin Y, Ren Q, Liu J, Zhang Y, Zheng H and Zhao P 2022 Exp. Mech. 62 761
- [43] Que Y, Xiao W, Fei X, Chen H, Huang L, Du S X and Gao H J 2014 Appl. Phys. Lett. 104 093110
- [44] Lu J, Neto A H and Loh K P 2012 Nat. Commun. 3 823
- [45] Ding P, Yan J, Wang J, Han X, Yang W, Chen H, Zhang D, Huang M, Zhao J, Yang S, Xue T T, Liu L, Dai Y, Hou Y, Zhang S, Xu X, Wang Y and Huang Y 2024 Nano Lett. 24 8208